Snake Robot With Opposing Helix Gait for Transporting Cylindrical Objects

Kiyoshiro Miki, Ching Wen Chin, *Graduate Student Member, IEEE*, and Motoyasu Tanaka, *Member, IEEE*

***Abstract*—In this study, we designed an opposite helix gait for object transportation using a non-wheeled snake robot. The proposed gait enables straight motion, turning motion, and pivot turning motion, allowing the robot to transport objects without ground contact. The target shape of the proposed gait features helices facing each other in a distinctive configuration. An elliptical helix, with its height defined by arc length, was designed for turning motion. By utilizing the proposed shape and employing rolling motion, opposing forces can be generated. This enables pivot turning motion—a capability difficult for conventional snake robots—and allows for compensation of the relative position between the robot and the object through object position manipulation. We conducted actual robot experiments for each type of motion and object transportation to verify the effectiveness of the proposed method. In particular, the trajectories of straight, turning, and pivot turning motions were measured and compared with theoretical predictions.**

***Index Terms*—Redundant robots, grasping, snake-like robot, locomotion, transportation.**

I. Introduction

IN DISASTER sites and environments difficult for humans to access, it is often preferable for robots, rather than humans, to replace or assist with tasks, from the perspectives of safety and operational efficiency. For example, in disaster areas such as earthquakes, fires, and nuclear power plant accidents, multiple risks exist, including toxic substances, risk of collapse, poor visibility, etc. and thus the introduction of robot technology is attracting attention as a means to conduct investigations and operations without endangering human lives.

One type of robot expected to be applied in such extreme environments is the snake robot [1]. Snake robots, composed of numerous degrees of freedom, can exhibit high mobility even in narrow spaces like pipes or complex environments such as uneven ground, where conventional wheeled robots or multi-legged robots struggle to cope. Snake robots are broadly classified into two types: wheeled and non-wheeled. Among the gaits of snake robots, those replicating natural snake movements include sidewinding and sinus-lifting [2], as well as obstacle-aided locomotion [3]. Demonstrating their adaptability, researchers have developed gaits for real-world environments, such as pipe-traversal for uneven terrain [4], external pipe navigation [5], and aquatic propulsion [6]. Unique propulsion methods for snake robots have also been proposed, including torsional rolling [7], crawler-gait [8], and COG (Center of Gravity) shift locomotion [9]. Furthermore, methods for seamless gait transitions between different environments [10] and for modeling these gaits [11] have been proposed.

Meanwhile, studies on object transportation by snake robots are also advancing. For example, methods have been proposed for pushing objects on the ground using the head and tail of a passive-wheeled snake robot [12] and for encircling and transporting objects using the torso of the non-wheeled snake robot [13], [14]. Furthermore, control methods enabling grasping and transportation with wheeled snake robots equipped with a soft gripper [15], methods for cooperative lifting and transportation by multiple wheeled snake robots [16], [17], and approaches for grasping and transportation using arms or attachments on non-wheeled snake robots [18], [19] have also been proposed.

Transportation that relies solely on the morphological structure of a single snake robot [12], [13], [14] is limited to scenarios where the transported object remains in contact with the ground. Under such conditions, challenges arise, including the risk of object damage due to interaction between the object and the ground, as well as susceptibility to obstacles such as friction and steps. Conversely, methods employing grippers or attachments [15], [18], [19] allow for object lifting and facilitate manipulation. However, they may lead to increased mechanical complexity or impose constraints on the objects being transported.

However, no studies have investigated single snake robots that transport objects lifted off the ground without arms or attachments. It requires a gait design that enables manipulation to prevent the object from being dropped and also allows for propulsion, presenting significant challenges for its realization. If this challenge is overcome, it is expected to broaden the range of tasks that snake robots can adapt to, leading to the development of more advanced and multi-functional operations. In this study, we aim to realize the transportation of objects lifted off the ground using a single non-wheeled snake robot. Section II presents a gait design that enables straight motion, turning, and pivot turning, together with corrective motions to continuously grasp the object. Section III evaluates, through real-world experiments, each motion's success rate and travel distance and verifies the effectiveness of the proposed method.

Received 24 July 2025; accepted 30 November 2025. Date of publication 17 December 2025; date of current version 31 December 2025. This article was recommended for publication by Associate Editor K. Tahara and Editor C. Gosselin upon evaluation of the reviewers' comments. This work was supported by JSPS KAKENHI under Grant JP25K01195. *(Corresponding author: Motoyasu Tanaka.)*

The authors are with the Department of Mechanical and Intelligent Systems Engineering, The University of Electro-Communications,, Tokyo 182-8585, Japan (e-mail: kiyoshiro.miki@rc.mce.uec.ac.jp; chin.ching.wen@rc.mce.uec.ac.jp; mtanaka@uec.ac.jp).

This article has supplementary downloadable material available at https://doi.org/10.1109/LRA.2025.3645515, provided by the authors.

Digital Object Identifier 10.1109/LRA.2025.3645515

2377-3766 © 2025 IEEE. All rights reserved, including rights for text and data mining, and training of artificial intelligence and similar technologies. Personal use is permitted, but republication/redistribution requires IEEE permission. See https://www.ieee.org/publications/rights/index.html for more information.

Authorized licensed use limited to: NANKAI UNIVERSITY. Downloaded on January 29,2026 at 13:05:37 UTC from IEEE Xplore. Restrictions apply.

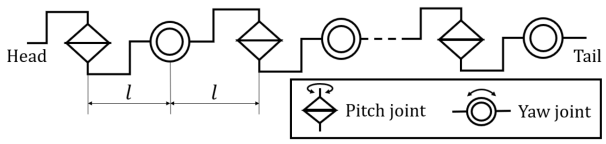

Fig. 1. Structure of the snake robot.

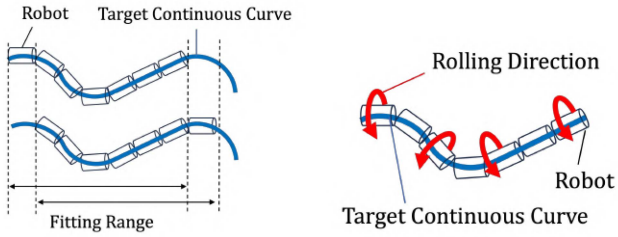

(a) Shift motion (b) Rolling motion

Fig. 2. Snake robot motions.

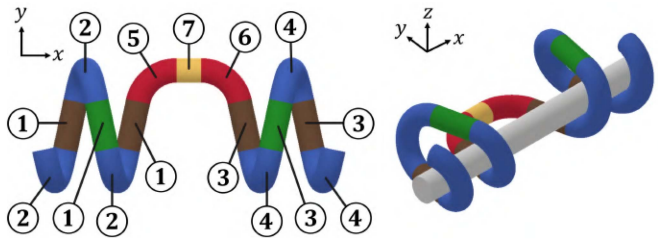

(a) Top view (b) Perspective view

Fig. 3. Target shape.

II. Gait Design and Control Method for Object Transportation

The non-wheeled snake robot used in this study, depicted in Fig. 1, consists of pitch and yaw joints connected alternately.

In the control of snake-like robots, we employ the continuous curve approximation method proposed by Yamada et al. [20], and the curve connection method extended by Takemori et al. [8]. These methods allow the design of target shapes by connecting curves with known curvature and torsion. Each simple curve is referred to as a segment and each segment is connected with relative torsion angle. The robot is then fitted to the composite curve. Here, changing the range of the target curve to which the robot is fitted is referred to as a shifting motion, while rotating the robot about its body axis is called a rolling motion. Examples of each motion are shown in Fig. 2.

A. Shape for Object Transportation

We propose the target shape for object transportation shown in Fig. 3(a), with parameters listed in Table I. The object to be manipulated is cylindrical and is grasped and transported by enclosing it with the robot body, as shown in Fig. 3(b). Segments ①, ③, and ⑦ are straight, with the length l_{pr}, l_{pl}, and l_c, respectively. Segments ② and ④ are helix, with r_{pr} and r_{pl} as their helical radii, h_{pr} and h_{pl} as their pitch parameters, and their central angles are both π. Segments ⑤ and ⑥ are circular arc, with l_{cr} and l_{cl} as their arc lengths, and θ_{cr} and θ_{cl} as their central angles. The propulsion part is composed of straight segments ① and ③, along with helix segments ② and ④. The

TABLE I
Parameters of Each Segment

Segment	Shape	Parameters
① (Propulsion Part)	Straight	$l_1 = l_{pl}$
② (Propulsion Part)	Helix	$(r_2, h_2, \phi_2) = (r_{pl}, h_{pl}, \pi)$
③ (Propulsion Part)	Straight	$(l_3) = l_{pr}$
④ (Propulsion Part)	Helix	$(r_4, h_4, \phi_4) = (r_{pr}, h_{pr}, \pi)$
⑤ (Connection Part)	Circular arc	$(l_5, \phi_5) = (l_{cl}, \theta_{cl})$
⑥ (Connection Part)	Circular arc	$(l_6, \phi_6) = (l_{cr}, \theta_{cr})$
⑦ (Connection Part)	Straight	$l_7 = l_c$

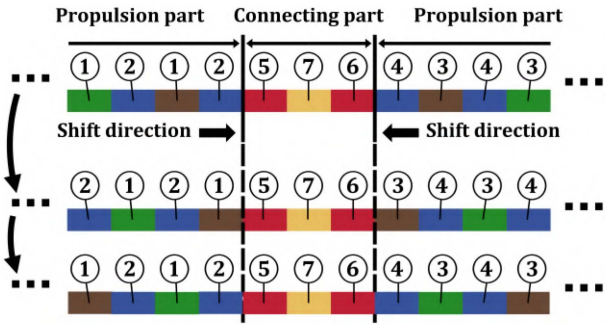

Fig. 4. Shift direction.

connecting part is composed of circular arc segments ⑤ and ⑥ and straight segment ⑦. The propulsion part is divided into a left propulsion part consisting of ① and ②, and a right propulsion part consisting of ③ and ④. The helix axes of helix segments ② and ④, which have opposite winding directions in the left and right propulsion parts, are connected by the connecting part so that they coincide.

In the proposed gait, shift motion is performed such that the left and right propulsion parts face each other, as illustrated in Fig. 4. Each propulsion part consists of a repetitive sequence of straight and helical segments, and locomotion is achieved by shifting only these segments. Here, the portion of the robot that is fitted to the connecting part remains fixed.

To align the helix axes directions of the left and right propulsion parts, torsion angles of $\pi/2$ and $-\pi/2$ are applied, respectively, to the terminal points of the connecting part that interface with the propulsion parts. The central angles θ_{cr} and θ_{cl} of circular arc segments ⑤ and ⑥ in the connecting part are calculated by the following equations:

$$\begin{bmatrix} \theta_{cl} \\ \theta_{cr} \end{bmatrix} = \begin{bmatrix} \left| \arctan\left(\dfrac{r_{pl}}{h_{pl}}\right) \right| \\ \left| \arctan\left(\dfrac{r_{pr}}{h_{pr}}\right) \right| \end{bmatrix} \tag{1}$$

As shown in Fig. 5, the circular arcs ⑤ and ⑥ in Fig. 3(a) may penetrate the ground. To minimize this, it is desirable for circular arcs ⑤ and ⑥ to be segments of short length. Since turning and pivot motions require parameter adjustments, we use circular arcs of fixed length but variable central angle. The arc lengths are set to $l_{cl} = l_{cr} = 2l$, l is the robot's link length.

B. Straight Motion

For straight motion, the target curve is designed to be symmetrical from left to right. Specifically, parameters are set such that $l_{pr} = l_{pl}$, $r_{pr} = r_{pl}$, and $h_{pr} = -h_{pl}$. Straight motion is

Authorized licensed use limited to: NANKAI UNIVERSITY. Downloaded on January 29,2026 at 13:05:37 UTC from IEEE Xplore. Restrictions apply.

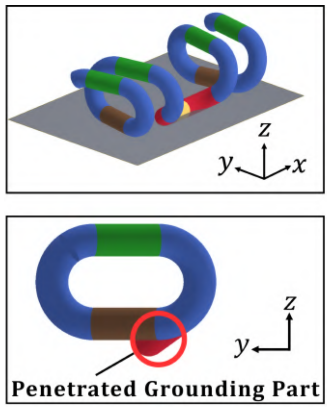

Fig. 5. Ground penetration.

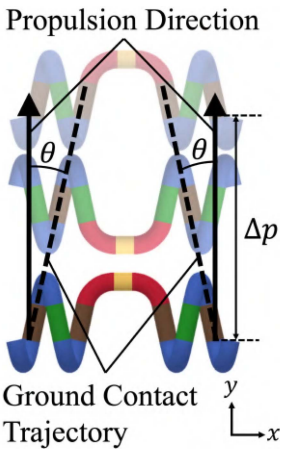

Fig. 6. Straight motion.

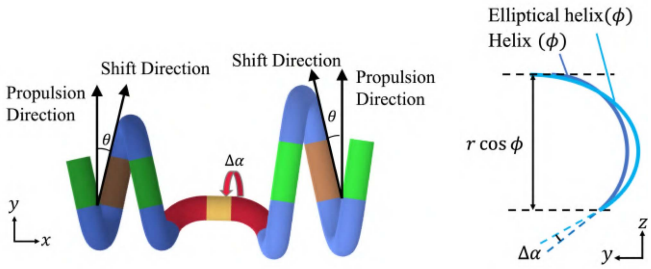

Fig. 7. Turning motion. (a) Target shape. (b) Helix and elliptical helix.

achieved by independently performing shift motion for the left and right propulsion parts. Fig. 6 shows that the robot is propelled forward through shift motion. For reference, the propulsion distance Δp on a no-slip condition between the robot and the ground is derived from the shift amount Δs, as follows,

$$\Delta p = \Delta s \cos\theta \tag{2}$$

C. Turning Motion

As shown in Fig. 7(a), turning motion is achieved by changing the length of each segment in the left and right propulsion parts and varying the shift amount. If a helix segment is scaled by a factor of c in either propulsion part, the resulting height difference between the left and right propulsion parts causes the robot body to tilt upon ground contact. To equalize the heights of the left and right propulsion parts, we propose an elliptical helix with the major axis b, minor axis r_p, and the helical height per unit arc length h_p. For example, assuming the left propulsion part as the reference, the elliptical helix for the right side is defined as follows, where ϕ represents the central angle:

$$\begin{bmatrix} x \\ y \\ z \end{bmatrix} = \begin{bmatrix} -h_{pr}\int_0^{\phi}\sqrt{\left(\frac{dy}{d\phi}\right)^2+\left(\frac{dz}{d\phi}\right)^2}\,d\phi \\ b\sin(\phi) \\ r_{pr}\cos(\phi) \end{bmatrix} \tag{3}$$

Hereby, h_{pr} and r_{pr} are defined as follows,

$$r_{pr} = r_{pl} \tag{4}$$

$$h_{pr} = \frac{h_{pl}}{\sqrt{r_{pl}^2+h_{pl}^2}} \tag{5}$$

The major axis b of the elliptical helix is computed numerically from the following equation:

$$c\pi\sqrt{r_{pl}^2+h_{pl}^2} = \int_0^{\pi}\sqrt{\left(\frac{dx}{dt}\right)^2+\left(\frac{dy}{dt}\right)^2+\left(\frac{dz}{dt}\right)^2}\,dt \tag{6}$$

In the proposed method, two propulsion parts are connected via a connecting part, where the straight segment is constrained along the helix axis direction of the propulsion parts. By using the proposed elliptical helix, where the helical height is defined based on the arc length, the angle between any point on the elliptical helix and the helix axis remains constant. This property simplifies the determination of the central angle θ_c for the circular arc in the connecting part.

As shown in Fig. 7(b), the z-coordinates of both the helix and the elliptical helix are identical with respect to the central angle ϕ, allowing a target body shape to be defined by aligning their central angles. However, since the tangential directions at the contact points differ between the two helices, the connecting part was adjusted to align these directions. Let the tangential angles of the circular helix and the elliptical helix be denoted by α_l and α_r. Then, the correction angle $\Delta\alpha$ for aligning tangential directions in the yz-plane is given by:

$$\Delta\alpha = \alpha_l - \alpha_r \tag{7}$$

Here, α_l and α_r are obtained, respectively, by the following equations:

$$\alpha_l = \arctan\left(-\frac{\cos\theta}{\sin\theta}\right) \tag{8}$$

$$\alpha_r = \arctan\left(-\frac{b\cos\theta}{r_{pl}\sin\theta}\right) \tag{9}$$

To correct the tangential mismatch between the circular helix and the elliptical helix, a torsion angle of $\Delta\alpha$ is applied to the torsional angle between the straight and circular arc segments of the connecting part, as shown in Fig. 7(a).

D. Pivot Turning Motion

As shown in Fig. 8, the target curve is configured so that the angle between the propulsion part and connecting parts is adjusted, the grounded straight segments align with the propulsion

Authorized licensed use limited to: NANKAI UNIVERSITY. Downloaded on January 29,2026 at 13:05:37 UTC from IEEE Xplore. Restrictions apply.

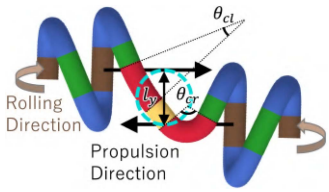

Fig. 8. Pivot turning motion view.

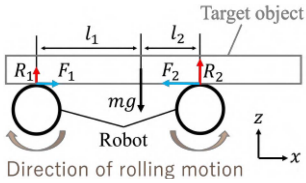

Fig. 9. Correction motion view.

direction, Pivot turning motion is executed when the connecting part contacts the straight segment of the robot's upper propulsion part. Meanwhile, the left and right propulsion parts slide along the y-axis. When a rolling motion is applied in this configuration, the propulsive forces from the left and right propulsion parts, indicated by black arrows, generate a moment inducing a pivot turning. Here, the parameters of the circular arc segments of the connecting part are defined by the following equation, where the angle change $\Delta\theta_c$ offsets the propulsion part:

$$\begin{bmatrix}\theta_{cl}\\ \theta_{cr}\end{bmatrix} = \begin{bmatrix}\left|\arctan\left(\frac{r_{pl}}{h_{pl}}\right) - \arctan\left(\frac{h_{pl}}{r_{pl}}\right)\right| - \Delta\theta_c\\ \left|\arctan\left(\frac{r_{pr}}{h_{pr}}\right) - \arctan\left(\frac{h_{pr}}{r_{pr}}\right)\right| + \Delta\theta_c\end{bmatrix} \quad (10)$$

E. Correction Motion by Rolling

Among the rolling motions of the proposed body shape, the motion in the direction shown in Fig. 9 is referred to as inward rolling motion. It is used to correct the relative position between the robot body and the object. Here, considering the case where the object is grasped at one point on each of the left and right propulsion parts, utilizing the grounded straight segments of the robot body. Assuming the mass of the grasped object is m, and the lengths from the center of gravity to the robot body on the right and left sides are l_1 and l_2 respectively, the reaction forces R_1 and R_2 received by the object from the robot body are:

$$R_1 = \frac{l_2}{l_1 + l_2}mg, \quad R_2 = \frac{l_1}{l_1 + l_2}mg \quad (11)$$

The forces F_1 and F_2, generated by the rolling motion at the contact points between the robot body and the object, act in the direction of the arrows with magnitudes of $R_1\mu'$ and $R_2\mu'$ respectively. where μ' is the coefficient of kinetic friction. For example, when $l_1 > l_2$ and thus $R_1 < R_2$, the object moves until l_1 and l_2 become equal. When $l_1 = l_2$, the forces generated by inward rolling motion are balanced, resulting in a stationary state of the object, thereby maintaining the relative center position.

F. Fitting Method for Reducing Discretization Error

Discretization errors arise when fitting the robot's joint angles to a target curve. In particular, if the fitted joint configuration is asymmetrical between the left and right propulsion parts, the robot's body shape may become significantly distorted. To address this issue, the fitting is performed so that the joint configuration becomes symmetrical with respect to the straight segment of the connecting part, as illustrated in Fig. 10. This symmetry ensures that identical discretization errors, occur equally on both sides. As a result, the overall body shape of the robot remains stable and free from significant distortion.

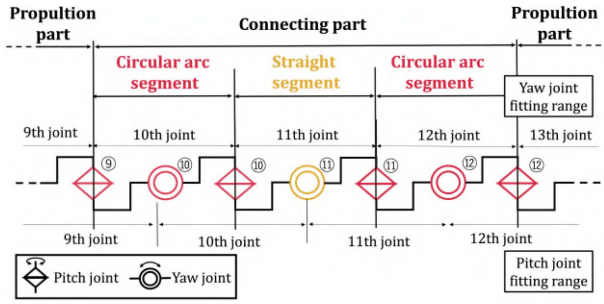

Fig. 10. Fitting around the connecting part.

TABLE II
PARAMETERS FOR STRAIGHT MOTION EXPERIMENTS.

Case	l_p [m]	r_p [m]	h [m/rad]	l_c [m]	r_c [m]	$l_{g\,\min}$ [m]
1	0.07	0.08	0.025	0.14	0.14	0.021
2	0.14	0.08	0.025	0.21	0.14	0.038
3	0.14	0.08	0.025	0.14	0.14	0.043

Fig. 11. (a) Snake robot. (b)(c) Target transported object.

III. EXPERIMENT

Experiments were conducted for each proposed motion based on the parameters listed in Table II. The snake robot and the object to be transported are shown in Fig. 11. Two sizes of rigid PVC pipes were used as the transported objects as shown in Fig. 11(b)(c). The diameter and the mass of the pipes are 76 mm, 1350 g and 89 mm and 1100 g, respectively. The robot body was developed by Takanashi et al. [22], utilizing the pectinate structure devised by Takemori et al. [21], which enables the robot to maintain a smooth body surface throughout its joint range of motion from $-\pi/2$ to $\pi/2$ rad. The robot has 40 joints, a link length l of 70 mm, a link radius of 28 mm, and each link weighs 146 g. The system was powered and controlled using a laptop computer and a 30 V DC power supply. Here, one cycle is defined as a shift motion passing through two straight segments and two helical segments of the propulsion part. The motion was performed at a rate of one cycle every 8 seconds.

Authorized licensed use limited to: NANKAI UNIVERSITY. Downloaded on January 29,2026 at 13:05:37 UTC from IEEE Xplore. Restrictions apply.

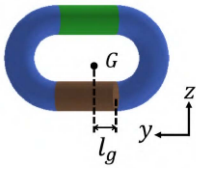

Fig. 12. Definition of l_g.

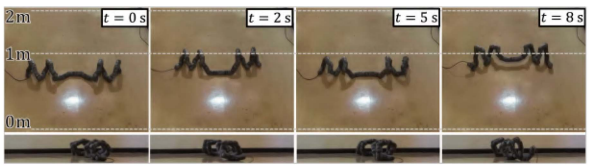

(a) Case 1: Unsuccessful propulsion

(b) Case 2: Unsuccessful propulsion

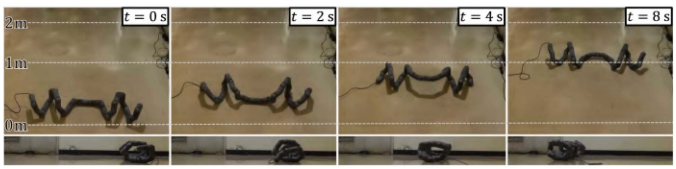

(c) Case 3: Successful propulsion

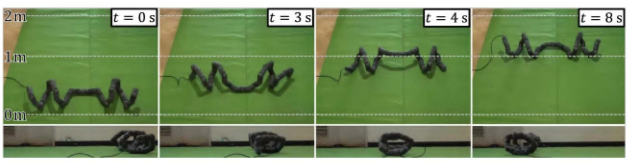

(d) Case 3: Successful propulsion (high friction)

Fig. 13. Straight motion experiments.

We define l_g as the distance in the y-direction between the trailing edge of the rear grounding part and the Center of Gravity(COG), as illustrated in Fig. 12. Although the COG varies with robot's body shape, we denote $l_{g\min}$ as the minimum l_g attained during the motion and use this value to characterize the shape parameters.

In addition, as an index for evaluating body shape deviation during the motion, we define D as the mean difference, over control cycles and joints, between the target joint angle and the measured joint angle one control cycle later. In our experiments, an angular velocity is issued at every control cycle to cancel the error between the current and target angles. If the body shape is maintained without deviation, the next-cycle measured angle coincides with the current target angle. Hence, a larger D indicates a greater body shape deviation over the motion.

A. Straight Motion

The straight motion is conducted using the parameter sets as stated in Table II. Unsuccessful propulsion may have occurred, and the robot rotated on the spot as shown in Fig. 13. The success rate was 0 in Case 1 and 0.6 in Case 2, and 0.867 in Case 3. This is because the proposed method is highly sensitive to the COG location. When the COG is rear-biased, the joints at the rear of the robot cannot be lifted, as illustrated in Fig. 14; instead, the front joints are lifted, and propulsion cannot proceed as intended. In contrast, propulsion proceeds as desired with front-biased COG. Thus, Case 3 with the largest $l_{g\min}$ has the highest success rate.

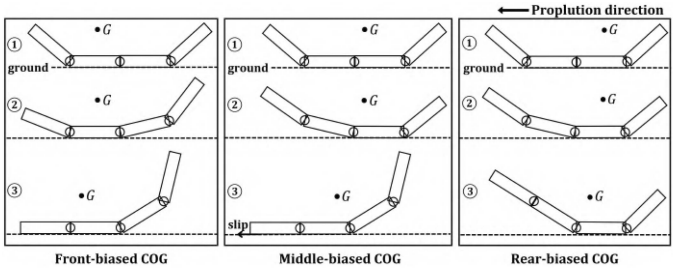

Fig. 14. Relationship between center of gravity position and propulsion.

TABLE III
RESULT OF STRAIGHT MOTION.

Condition	Speed [s/cycle]	Success rate	$\bar{p_s}$ [mm]	$s^2_{p_s}$ [mm^2]	D [$\times 10^{-3}$ rad]	P [mm]
Low friction	8	0.867	859.9	15.89	0.6895	769
Low friction	4	1	858.7	17.56	0.6189	769
High friction	8	1	842.6	18.93	0.8242	769
High friction	4	1	865.3	19.86	2.291	769

In addition, under the Case 3 parameters, we varied the shift speed and floor friction conditions, and measured the travel distance per cycle using a motion capture. We computed the mean travel distance $\bar{p_s}$, its variance $s^2_{p_s}$, and the theoretical value P from (2). The results are compared in Table III. For each condition, we performed five sets of straight motion trials, each lasting three cycles. Representative snapshots of the experiments are shown in Fig. 13. The success rates were higher under conditions of increased speed and friction. A greater speed provides the momentum for the robot to propel forward. Moreover, penetration of the connecting part into the ground (Fig. 5) can induce upward lifting motions at the front of robot and may lead to propulsion failure. In high friction environments, penetration of the connecting part into the ground that is accompanied by sliding is considered less likely to occur. Because D is larger under high friction, indicating a deviation from the target body shape, it is inferred that ground penetration becomes less likely and, consequently, the success rate increases.

There was a discrepancy between the P and $\bar{p_s}$ under all conditions. This discrepancy is likely due to the COG being located near the midpoint between the front and rear, causing the front part of the robot to temporarily lift, as shown in Fig. 14, and then forcefully strike the ground, resulting in slippage. Additionally, when the connecting part penetrates the ground, it acts as a fulcrum and propels the robot forward. Unintended propulsion may also occur due to rolling when the head is fitted within the helical segments. Note that the torsional angle varies along the helical segments. Thereby, when the head is fitted in the helical segment, the torsional angle of the head changes during shift motion, thus resulting the unintended rolling motion. These

Authorized licensed use limited to: NANKAI UNIVERSITY. Downloaded on January 29,2026 at 13:05:37 UTC from IEEE Xplore. Restrictions apply.

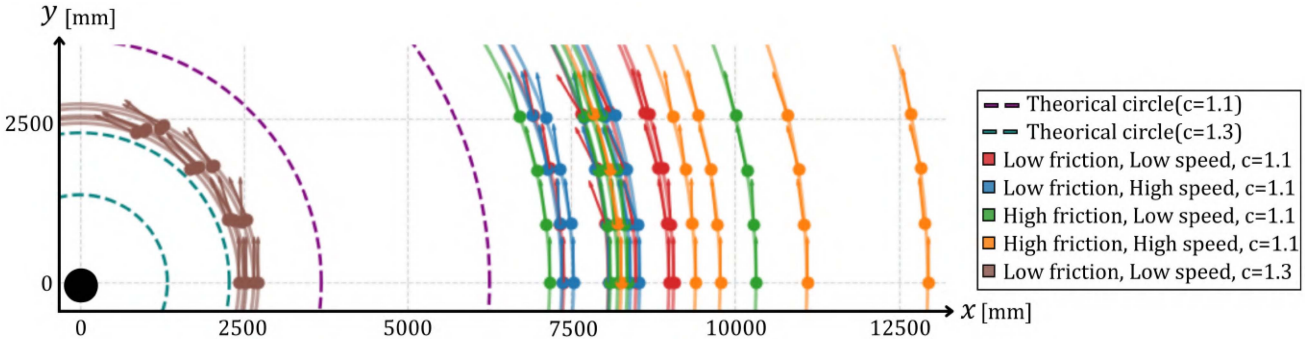

Fig. 15. Trajectory of turning motion.

TABLE IV
RESULT OF TURNING MOTION.

Condition	Speed s/cycle	c	$\bar{r}$ [mm]	s_r^2 [mm^2]	D [$\times 10^{-3}$ rad]	R ($d_{\max}$)	R ($d_{\min}$)
Low friction	8	1.1	8398	623	0.3009	6252	3683
Low friction	4	1.1	7982	468	1.744	6252	3683
High friction	8	1.1	8430	1033	1.962	6252	3683
High friction	4	1.1	10276	1616	1.380	6252	3683
Low friction	8	1.3	2566	105	0.9549	2279	1332

factors are thought to lead to the discrepancy with the theoretical value.

On a low friction floor surface, there was almost no difference in the propulsion distance $\bar{p}_s$ on different shift speed, but in high friction environments, $\bar{p}_s$ was larger on higher shift speed. This is considered to be due to the aforementioned connecting part penetrating the ground, and the decrease in slippage caused by the increased ground friction as shown in Fig. 14. It was found that the value D was the largest under the high friction environment with high shift speed. This indicates that the deviation of the body shape was very significant, which resulted in a change in interaction with the ground, and thus an alteration in the propulsion distance. Furthermore, $s_{p_s}^2$ also tended to increase as the speed or friction increased. This shows that the lower shift speed and lower-friction environment provide a stable and reproducible propulsion.

B. Turning Motion

Turning motion experiments were conducted with varied floor friction conditions, shift speed, and the length ratio c between the left and right propulsion parts. The parameters of Case 3 from previous were used and $c = 1.1$ and $c = 1.3$ were compared. The travel path of each cycle was measured using a motion capture and the radius of the circular path were calculated. Five sets of three cycles of turning motion were performed for each condition. The average radius of circular path $\bar{r}$ and the variance s_r^2 were calculated for each set, and compared with the theoretical value R. The experimental results are presented in Table IV and Fig. 15.

The case of a two-wheeled drive system is taken as a comparison, as shown in Fig. 16. The velocities of the right v_R and left v_L wheels can be expressed in relation to the turning radius R and the half-distance between the wheels d by the following equations:

$$v_R = (R + d)\omega \tag{12}$$

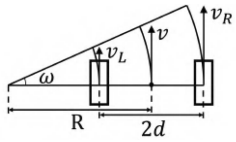

Fig. 16. Two-wheel drive turning.

$$v_L = (R - d)\omega \tag{13}$$

From these equations, the turning radius R can be derived as:

$$R = \frac{d(v_R + v_L)}{v_R - v_L} \tag{14}$$

This result can be applied to the proposed turning motion by assuming the distance between the robot's grounding parts is $2d$, and $v_R = cv_L$, the turning radius R is obtained as:

$$R = \frac{d(c+1)}{2(c-1)} \tag{15}$$

In the turning motion, the grounding part is a line rather than a point, and furthermore, because the distance between the grounding part constantly changes, the theoretical value of the turning radius cannot be uniquely determined. Here, d_{min} and d_{max} are introduced, where d_{min} is the length only considering the connecting part and d_{max} is the length considering both the connecting part and the helical segments next to it. The theoretical minimum and maximum turning radii are obtained, using d_{min} and d_{max} respectively.

The experimental results show that the measured values exceeded the theoretical values in all cases, as shown in Fig. 15. The robot was generally oriented in the tangential direction of the estimated circular path, which shows the robot was turning. This is likely attributable to the fact that, the actual grounding part is a straight line rather than a point contact, where slippage is unavoidable in turning motion. However, modeling the slip regions along the grounding straight line is challenging. To predict the turning radius more accurately, it is necessary to account for the continuously changing distribution of frictional forces along the contact area. The deviation from the theoretical value was found to be smaller when $c = 1.3$ than when $c = 1.1$. This is likely because a larger speed difference between the left and right sides increases the required slip of the grounding segments for turning, thereby suppressing stick–slip. A similar behavior is observed in the turning motion of crawler robots.

Furthermore, possible reasons for the variation in turning radius depending on shift speed and ground friction are discussed.

Authorized licensed use limited to: NANKAI UNIVERSITY. Downloaded on January 29,2026 at 13:05:37 UTC from IEEE Xplore. Restrictions apply.

TABLE V
RESULT OF PIVOT TURN MOTION

Condition	$\bar{\theta}_p$ [rad]	$s^2_{\theta_p}$ [rad^2]	$\bar{p}_p$ [mm]	$s^2_{p_p}$ [mm^2]	θ_P [rad]
Low friction	1.167	0.08524	223.3	52.36	3.620
High friction	0.9613	0.1093	144.1	26.01	3.620

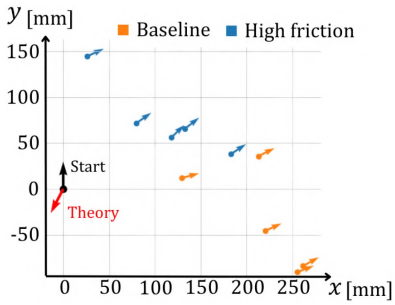

Fig. 17. The position and orientation of the COG after pivot turning.

Slippage between the body and the ground is essential for turning motion. However, the value of D changes significantly compared to straight motion, which suggests that the way the body shape collapses also varies substantially depending on the shift speed and ground friction conditions. As a result, the torque required for each joint to maintain the body shape differs throughout the conditions, affecting the pattern of slippage and ultimately the resulting turning radius. It is difficult to precisely predict the behavior from these complex conditions of slippage and friction. Therefore, an appropriate feedback control is required in the future.

C. Pivot Turning Motion

The experiment was conducted using Case 3 parameters, where the propulsion part was offset by an angle of $\Delta\theta_c = \pi/3$ rad. Each experiment involved a rolling motion corresponding to a total of 10π radians of rotation and was performed five times for each floor friction condition. The robot's movement was tracked using a motion capture system, and the average rotational angle $\bar{\theta}_p$ and travel distance $\bar{p}_p$, as well as their respective variances $s^2_{\theta_p}$ and $s^2_{p_p}$, were compared. The experimental results are presented in Table V and Fig. 17.

Here, it is assumed that the propulsion force due to rolling causes the robot to move along a circular path whose diameter is equal to the y-direction distance l_y between the centers of the grounded straight segments, as illustrated by the dashed circle in Fig. 8. The theoretical turning angle θ_P is then given by the following equation:

$$\theta_P = \frac{\Delta\psi\, a}{\pi l_y} \tag{16}$$

where $\Delta\psi$ is the rolling amount during the pivot turning motion.

Note that the slippage during the pivot turning is not considered in the theoretical value. However, slippage between the body and the ground is essential and significant for the pivot turning motion; thus, the deviation of $\bar{\theta}_P$ from θ_P was very large. $\bar{\theta}_P$ was larger, and the robot was able to rotate more in the low friction condition. However, a larger displacement was also observed on low friction condition because the motion was larger on the slippery surface. In the high friction condition, $\bar{\theta}_P$ was smaller and $s^2_{\theta_P}$ was larger. This is due to the slippage between the robot and ground being more unpredictable.

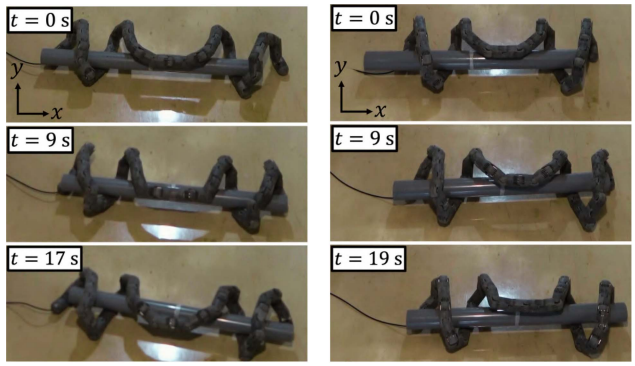

(a) Smaller object (b) Larger object

Fig. 18. Correction motion experiments.

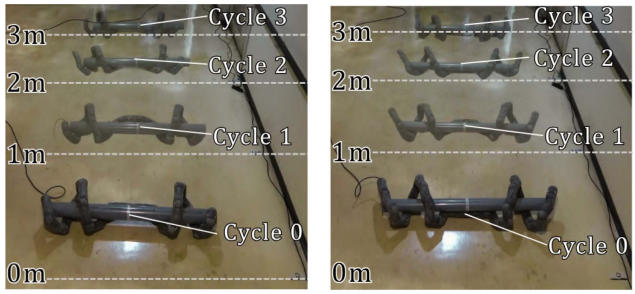

(a) Smaller object (b) Larger object

Fig. 19. Straight motion experiments

D. Correction Motion and Object Transportation

Both the objects in Fig. 11 were transported using Case 3 parameters, except $r_p = 0.09$ m for Fig. 11(c). The correction motion successfully reduced the relative center position between the robot and the object in both cases, as shown in Fig. 18. Note that the grounding segments of the propulsion parts are nonparallel in the correction motion. As a result, a slight movement of the robot along the negative y-axis was observed as a side effect of the correction motion. Moreover, a slight movement along the positive x-axis was caused by the imbalanced normal forces on the grounding segments. In addition, straight, turning, and pivot turning motions were executed, and their effectiveness was confirmed for both objects. Fig. 19 shows straight motion performed over three cycles while grasping an object. The robot was able to propel forward while transporting the object in both cases. Fig. 20 illustrates the robot grasping an object and executing a turning motion. $c = 1.3$ is used for the larger object and $c = 1.1$ is used for the smaller object. In both cases the robot completed three cycles with propulsion while turning and transporting the object. The case with $c = 1.3$ yielded greater turning. Fig. 21 shows a pivot turning motion using inward rolling while grasping the different size objects. The correction motion consistently stabilized the object's position, maintaining the relative alignment between the robot and the object. Additionally, since the transported object's weight was sufficiently

Authorized licensed use limited to: NANKAI UNIVERSITY. Downloaded on January 29,2026 at 13:05:37 UTC from IEEE Xplore. Restrictions apply.

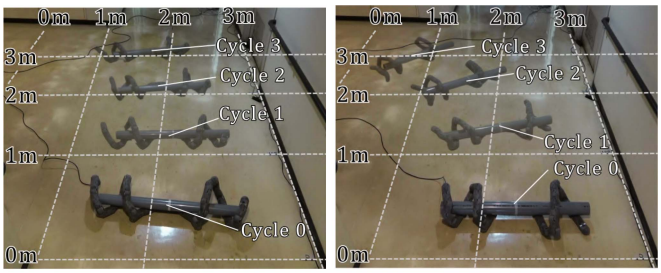

(a) Smaller object ($c = 1.1$) (b) Larger object ($c = 1.3$)

Fig. 20. Turning motion experiments

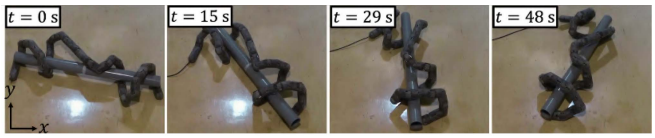

(a) Smaller object

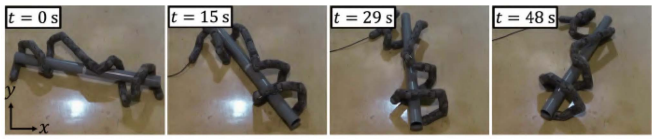

(b) Larger object

Fig. 21. Pivot turning motion experiments

small relative to that of the robot body, the frictional influence from the object is considered negligible.

IV. Conclusion

In this study, we proposed gait design for object transportation by a snake robot and verified its effectiveness through actual robot experiments. We investigated appropriate parameters for straight motion and confirmed that the intended propulsion could be achieved by adjusting the center of gravity position. In experiments of turning motion, the effectiveness of the proposed gait was confirmed as the robot's trajectory could be approximated to a circular path. The effectiveness of both pivot turning and correction motions was confirmed by performing rolling motion utilizing the proposed shape, which positions the left and right propulsion parts opposite each other. These motions collectively enabled the development of a gait that allows the snake robot to transport objects without dropping them on the ground. However, accurate prediction of the robot's behavior is difficult, and future work should focus on developing methods to obtain feedback. In addition, future efforts include implementing transition methods that enable smooth switching between straight, turning, and pivot turning motions, realizing pick up and placement motions for interacting with objects on the ground, and extending the system to handle transportation of objects beyond cylindrical shapes.

References

[1] J. Whitman, N. Zevallos, M. Travers, and H. Choset, "Snake robot urban search after the 2017 Mexico city earthquake," in *Proc. IEEE Int. Symp. Saf., Secur., Rescue Robot.*, 2018, pp. 1–6.

[2] R. Ariizumi and F. Matsuno, "Dynamic analysis of three snake robot gaits," *IEEE Trans. Robot.*, vol. 33, no. 5, pp. 1075–1087, Oct. 2017.

[3] A. A. Transeth, R. I. Leine, C. Glocker, K. Y. Pettersen, and P. Liljebäck, "Snake robot obstacle-aided locomotion: Modeling, simulations, and experiments," *IEEE Trans. Robot.*, vol. 24, no. 1, pp. 88–104, Feb. 2008.

[4] T. Baba, Y. Kameyama, T. Kamegawa, and A. Gofuku, "A snake robot propelling inside of a pipe with helical rolling motion," in *Proc. SICE Annu. Conf.*, 2010, pp. 2319–2325.

[5] T. Kamegawa, T. Harada, and A. Gofuku, "Realization of cylinder climbing locomotion with helical form by a snake robot with passive wheels," in *Proc. IEEE Int. Conf. Robot. Automat.*, 2009, pp. 3067–3072.

[6] S. Yu, S. Ma, B. Li, and Y. Wang, "An amphibious snake-like robot: Design and motion experiments on ground and in water," in *Proc. Int. Conf. Inform. Automat.*, 2009, pp. 500–505.

[7] W. Zhen, C. Gong, and H. Choset, "Modeling rolling gaits of a snake robot," in *Proc. IEEE Int. Conf. Robot. Automat.*, 2015, pp. 3741–3746.

[8] T. Takemori, M. Tanaka, and F. Matsuno, "Gait design for a snake robot by connecting curve segments and experimental demonstration," *IEEE Trans. Robot.*, vol. 34, no. 5, pp. 1384–1391, Oct. 2018.

[9] A. Yamano, Y. Ikeda, K. Imai, and M. Chiba, "Efficient rolling motion for snake-like robots utilizing center of gravity shift," *Mechatronics*, vol. 94, 2023, Art. no. 103024.

[10] T. Takemori, M. Tanaka, and F. Matsuno, "Hoop-passing motion for a snake robot to realize motion transition across different environments," *IEEE Trans. Robot.*, vol. 37, no. 5, pp. 1696–1711, Oct. 2021.

[11] W. Huang, Y. Fang, X. Guo, H. Liu, and L. Liu, "A unified motion modeling approach for snake robot's gaits generated with backbone curve method," *IEEE Trans. Robot.*, vol. 40, pp. 4132–4146, 2024.

[12] M. Nakajima, M. Tanaka, and K. Tanaka, "Simultaneous control of two points for snake robot and its application to transportation," *IEEE Robot. Automat. Lett.*, vol. 5, no. 1, pp. 111–118, Jan. 2020.

[13] A. Salagame et al., "Non-impulsive contact-implicit motion planning for morpho-functional loco-manipulation," in *Proc. IEEE Int. Conf. Adv. Intell. Mechatron.*, 2024, pp. 309–314.

[14] E. O. Ari, I. Erkmen, and A. M. Erkmen, "A FACL controller architecture for a grasping snake robot," in *Proc. IEEE/RSJ Int. Conf. Intell. Robots Syst.*, 2005, pp. 1748–1753.

[15] M. Tanaka, K. Tadakuma, M. Nakajima, and M. Fujita, "Task-space control of articulated mobile robots with a soft gripper for operations," *IEEE Trans. Robot.*, vol. 35, no. 1, pp. 135–146, Feb. 2019.

[16] M. Tanaka and F. Matsuno, "Cooperative control of two snake robots," in *Proc. IEEE Int. Conf. Robot. Automat.*, 2006, pp. 400–405.

[17] M. Tanaka and F. Matsuno, "Cooperative control of three snake robots," in *Proc. IEEE/RSJ Int. Conf. Intell. Robots Syst.*, 2006, pp. 3688–3693.

[18] S. Han et al., "Snake robot gripper module for search and rescue in narrow spaces," *IEEE Robot. Automat. Lett.*, vol. 7, no. 2, pp. 1667–1673, Apr. 2022.

[19] A. Salagame, K. Gangaraju, H. K. Nallaguntla, E. Sihite, G. Schirner, and A. Ramezani, "Loco-manipulation with nonimpulsive contact-implicit planning in a slithering robot," in *Proc. IEEE/RSJ Int. Conf. Intell. Robots Syst.*, 2024, pp. 309–314.

[20] H. Yamada and S. Hirose, "Study of active cord mechanism approximations to continuous curves of a multi-joint body," *J. Robot. Soc. Jpn.*, (in Japanese), vol. 26, no. 1, pp. 110–120, 2008.

[21] T. Takemori, M. Tanaka, and F. Matsuno, "Ladder climbing with a snake robot," in *Proc. IEEE/RSJ Int. Conf. Intell. Robots Syst.*, 2018, pp. 1–9.

[22] T. Takanashi, M. Nakajima, T. Takemori, and M. Tanaka, "Obstacle-aided locomotion of a snake robot using piecewise helixes," *IEEE Robot. Automat. Lett.*, vol. 7, no. 4, pp. 10542–10549, Oct. 2022.

Authorized licensed use limited to: NANKAI UNIVERSITY. Downloaded on January 29,2026 at 13:05:37 UTC from IEEE Xplore. Restrictions apply.